J. Fluid Mech. (2013), *vol.* 725, *pp.* 281–298. © Cambridge University Press 2013
doi:10.1017/jfm.2013.187

Spatial structure of spectral transport in two-dimensional flow

Yang Liao and Nicholas T. Ouellette†

Department of Mechanical Engineering and Materials Science, Yale University, New Haven, CT 06520, USA

(Received 26 October 2012; revised 8 April 2013; accepted 9 April 2013; first published online 14 May 2013)

Using filter-space techniques (FSTs), we study the spatial structure of the scale-to-scale flux of energy in two-dimensional flow. Analysing data from a weakly turbulent, experimental quasi-two-dimensional flow, we find rotationally symmetric patterns consisting of lobes of spectral flux of alternating sign that are associated with vortical motion in the flow field. Such patterns also occur in a simple analytical model, even though the single-scale model flow should have no scale-to-scale energy transfer. Thus, the interpretation of these alternating patterns must be handled with care. By decomposing the spectral flux into three distinct components, we show that these lobe patterns are entirely associated with the Leonard and, to a lesser extent, cross terms. In addition, we show that the contributions from these two terms are localized around the energy injection scale, and that the bulk of the inverse energy transfer in our flow is carried by the subgrid term alone.

Key words: isotropic turbulence, nonlinear dynamical systems, turbulent flows

1. Introduction

Nonlinear systems are characterized by a broadband spectral response to driving forces, since nonlinearities in the equations of motion become non-localities in Fourier space. Such a response is particularly prevalent in fluid flows when the Reynolds number, and therefore the relative strength of the nonlinearities, is large. In turbulent flow, the complex spectral behaviour self-organizes into a net transfer of energy from the large length and time scales at which it is injected to the small scales where it is dissipated: the famous Richardson–Kolmogorov energy cascade. In two dimensions, the energy cascade flips its direction and a second cascade, this one of enstrophy, emerges (Boffetta & Ecke 2012). Thus, even though the spectral structure of turbulence can be quite complex and can vary strongly from instant to instant, macroscopic features naturally and spontaneously emerge.

In a similar fashion, the spatial degrees of freedom of the flow field often spontaneously organize into distinguishable features, termed coherent structures (Hussain 1986). Little is known, however, about how these structures contribute to or participate in the rich spectral dynamics of the flow. Linking objects in real space and Fourier space is challenging, given that on the surface the two descriptions of the flow are incompatible.

† Email address for correspondence: nicholas.ouellette@yale.edu

https://doi.org/10.1017/jfm.2013.187 Published online by Cambridge University Press

In recent years, however, clever tools based on filtering (Germano 1992) have emerged that have begun to surmount these challenges. Using an approach that is conceptually similar to large eddy simulation (LES), we first remove information from the flow field by means of a spectral filter that suppresses motion at small scales (Meneveau & Katz 2000). By subsequently comparing the full velocity field (which, unlike in LES, we still retain) and the filtered field, we can extract information about their coupling and therefore about the transfer of energy and other quantities between them (Liu, Meneveau & Katz 1994; Eyink 1995). As we describe below, this approach, sometimes called a filter-space technique (FST) (Rivera *et al.* 2003), allows us to localize (at least approximately) these spectral transfer properties in space, opening the door to a wide range of new analysis possibilities.

FSTs have so far primarily been used to study the direct enstrophy and inverse energy cascades in two-dimensional turbulence (Kraichnan 1967; Leith 1967; Batchelor 1969). Rivera *et al.* (2003), for example, used them to study the spatial structure of the energy and enstrophy transfer in an experimental soap-film channel. They showed that even though the net spectral transfer measured in their experiment was in line with theoretical predictions, in that energy primarily flowed from the injection scale to larger scales and enstrophy to smaller scales, the flow displayed a significant amount of 'backscatter'; that is, large amounts of energy and enstrophy moved in the opposite direction from what was expected, and the net directionality of the cascades arose from significant cancellation. The results of Rivera *et al.* (2003) were confirmed and expanded upon by Chen *et al.* (2003) for the enstrophy cascade and Chen *et al.* (2006) for the inverse energy cascade using direct numerical simulation of the two-dimensional Navier–Stokes equations and experiments in an electromagnetically forced thin-layer flow. These studies probed the two cascades in more detail, and demonstrated local mechanisms that drove energy and enstrophy transfer to different length scales. Chen *et al.* (2003) showed, for example, that the direct enstrophy cascade originates from the enhancement of small-scale vorticity gradients by large-scale straining, and that the vorticity is primarily transported along streamlines rather than along the vorticity gradient. This result suggested that eddy-viscosity models of the enstrophy cascade must use a tensor rather than a scalar eddy viscosity. Subsequently, Chen *et al.* (2006) and Xiao *et al.* (2009) showed that the inverse energy cascade can be understood as a process where the large-scale strain stretches and weakens small-scale vortices. Again, however, a simple eddy-viscosity model could not capture their results; instead, the effective stress is oriented at 45° relative to the large-scale strain. They were also able to study the locality of the inverse cascade with these methods, finding that it is less local than the energy cascade in three-dimensional turbulence. FSTs were also used by Boffetta (2007) and Boffetta & Musacchio (2010) to analyse high-resolution numerical simulations of two-dimensional turbulence. They showed that the double-cascade scenario was robust at these very high resolutions, and additionally that the two cascades were relatively independent, in that intense energy and enstrophy fluxes were uncorrelated in space.

FSTs have also been used in Lagrangian studies. Wan *et al.* (2010), for example, found evidence for a Lagrangian energy cascade in three-dimensional turbulence by considering the Lagrangian correlation functions of viscous dissipation and scale-to-scale energy fluxes. They also observed an intriguing time delay between the Lagrangian correlation of the scale-to-scale energy flux and the energy dissipation. In two-dimensional weak turbulence, Kelley & Ouellette (2011*b*) showed that the scale-to-scale energy and enstrophy fluxes persist along the Lagrangian trajectories of fluid elements, with autocorrelation times that can be as long for the scale-to-scale

https://doi.org/10.1017/jfm.2013.187 Published online by Cambridge University Press

fluxes as they are for the velocity. In addition, these autocorrelation times were highly spatially heterogeneous, and their spatial structure was linked to hyperbolic and elliptic regions in the flow field.

Despite these successes, however, fields of the scale-to-scale fluxes computed via FSTs occasionally show unusual behaviour. For example, as we demonstrate in more detail below, they tend to show intense lobes of flux of alternating sign around vortex cores. These lobes are often some of the strongest fluxes in the field (Xiao *et al.* 2009), and yet their spatial average nearly vanishes, making their contribution to the dynamics somewhat unclear. In addition, as we show further below, non-vanishing spectral fluxes may appear when FSTs are applied even when the flow field has energy at only a single wavenumber.

To ensure the correct interpretation of the application of FSTs to experimental and numerical data, we have studied the behaviour of FSTs in detail in both a simple analytical example and in experimental data drawn from a quasi-two-dimensional flow experiment. We show that classic decompositions of the spectral flux fields separate the majority of the alternating lobe structures from the rest of the field, and may aid in interpretation. In § 2, we discuss the theoretical background for filtering and for the decompositions we will perform. We continue in § 3 by describing our experimental measurements, and show sample results that motivate our work. Before considering decompositions of the experimental fields, we present in detail a simple analytical example in § 4, where we take an analytically prescribed flow field with energy at only a single wavenumber and apply a FST. Then, in § 5, we discuss our experimental results in more detail. Finally, we summarize our findings and draw conclusions in § 6.

2. Theoretical background

The mathematics underlying a FST are straightforward. Here, we discuss the basic filtering operations we will perform and the interpretation of the resulting fields, as well as the decomposition we will use below in trying to understand the results more deeply.

2.1. *Filtering*

When we speak of filtering the velocity fields, we mean the removal of all of the high-wavenumber variation. The most straightforward way to do this is to convolve the field with a function that acts as a low-pass filter in Fourier space. We define a component of the filtered velocity field as

$$u_i^{(r)}(\boldsymbol{x}) \equiv \int G^{(r)}(\boldsymbol{x}-\boldsymbol{x}')u_i(\boldsymbol{x}')\,\mathrm{d}\boldsymbol{x}'. \tag{2.1}$$

Here $G^{(r)}$ is the filter kernel. In our notation, the superscript (r) denotes a quantity with all length scales smaller than r suppressed. We choose this notation as opposed to others (such as an overbar) common the LES literature to make it explicit what filter scale is chosen, since we will vary it. Unlike in LES, all scales are present in our data, and we will filter as a post-processing step.

Let us now consider the equation of motion for the filtered kinetic energy $E^{(r)} = (1/2)\,(u_i^{(r)})^2$. Taking the scalar product of the filtered, unforced Navier–Stokes equations with $u_i^{(r)}$, we obtain

$$\frac{\partial E^{(r)}}{\partial t} = -\frac{\partial}{\partial x_i}\left[\frac{1}{\rho}u_i^{(r)}p^{(r)} + u_i^{(r)}E^{(r)} - \nu\frac{\partial E^{(r)}}{\partial x_i} + u_j^{(r)}\tau_{ij}^{(r)}\right] - 2\nu s_{ij}^{(r)}s_{ij}^{(r)} + \tau_{ij}^{(r)}s_{ij}^{(r)}, \tag{2.2}$$

https://doi.org/10.1017/jfm.2013.187 Published online by Cambridge University Press

where $p^{(r)}$ is the filtered pressure, ρ is the fluid density, ν is the kinematic viscosity and $s_{ij}^{(r)} = (1/2)(\partial u_i^{(r)}/\partial x_j + \partial u_j^{(r)}/\partial x_i)$ is the rate of strain of the filtered velocity field. All of these quantities have clear analogues in the equation of motion for the full kinetic energy. But the tensor

$$\tau_{ij}^{(r)} = (u_i u_j)^{(r)} - u_i^{(r)} u_j^{(r)} \tag{2.3}$$

is new, and appears as a result of filtering the nonlinear term in the Navier–Stokes equations. In analogy with the standard Reynolds decomposition and with LES, we interpret $\tau_{ij}^{(r)}$ as a stress tensor that accounts for momentum transfer between the filtered velocity field and the small-scale part that we have removed. The inner product of $\tau_{ij}^{(r)}$ and $s_{ij}^{(r)}$, which appears in (2.2), gives the energy transfer between filtered and small-scale components. Thus, we can define the scalar field

$$\Pi^{(r)}(\boldsymbol{x}) = -\tau_{ij}^{(r)} s_{ij}^{(r)} = -\frac{1}{2}\left[(u_i u_j)^{(r)} - u_i^{(r)} u_j^{(r)}\right]\left[\frac{\partial u_i^{(r)}}{\partial x_j} + \frac{\partial u_j^{(r)}}{\partial x_i}\right] \tag{2.4}$$

to be the scale-to-scale energy flux through the filter scale r. With our sign convention, $\Pi^{(r)} > 0$ implies energy flux to smaller length scales (that is, from the filtered field to the small-scale field), while $\Pi^{(r)} < 0$ implies flux to larger scales (from the small-scale field to the filtered field).

2.2. *Flux decomposition*

As is well known in LES, the stress tensor $\tau_{ij}^{(r)}$ defined in (2.3) contains contributions from three logically distinct components, which can be distinguished based on considering the wavenumber triads that account for the scale-to-scale interactions (Pope 2000). Let us write the stress tensor as

$$\begin{aligned}\tau_{ij}^{(r)} = &\left\{(u_i^{(r)} u_j^{(r)})^{(r)} - u_i^{(r)} u_j^{(r)}\right\} \\ &+ \left\{(u_i^{(r)}(u_j - u_j^{(r)}))^{(r)} + (u_j^{(r)}(u_i - u_i^{(r)}))^{(r)}\right\} \\ &+ \left\{((u_i - u_i^{(r)})(u_j - u_j^{(r)}))^{(r)}\right\}.\end{aligned} \tag{2.5}$$

It is simple to show (noting that filtering distributes over addition) that this expression reduces to that given in (2.3). But the interpretation of the three terms in braces is different. The first is a small-scale quantity composed only of large-scale quantities; that is, it is a contribution to $\tau_{ij}^{(r)}$ coming purely from the filtered velocity field. In LES, this would be called a Leonard stress. The second term is a large-scale quantity built from one large-scale quantity ($u_i^{(r)}$) and one small-scale quantity ($u_i - u_i^{(r)}$). In LES, this would be called a cross stress. Finally, the last term is a large-scale quantity composed of two small-scale quantities, known as a subgrid stress in LES.

All three of these stresses contribute to the scale-to-scale energy flux $\Pi^{(r)}$, but their effects may be different. To isolate the three terms, we define

$$\Pi^{(r)} = \Pi_L^{(r)} + \Pi_C^{(r)} + \Pi_S^{(r)}, \tag{2.6}$$

with

$$\Pi_L^{(r)} \equiv -\left[(u_i^{(r)} u_j^{(r)})^{(r)} - u_i^{(r)} u_j^{(r)}\right] s_{ij}^{(r)} \tag{2.7}$$

$$\Pi_C^{(r)} \equiv -\left[(u_i^{(r)}(u_j - u_j^{(r)}))^{(r)} + (u_j^{(r)}(u_i - u_i^{(r)}))^{(r)}\right] s_{ij}^{(r)} \tag{2.8}$$

https://doi.org/10.1017/jfm.2013.187 Published online by Cambridge University Press

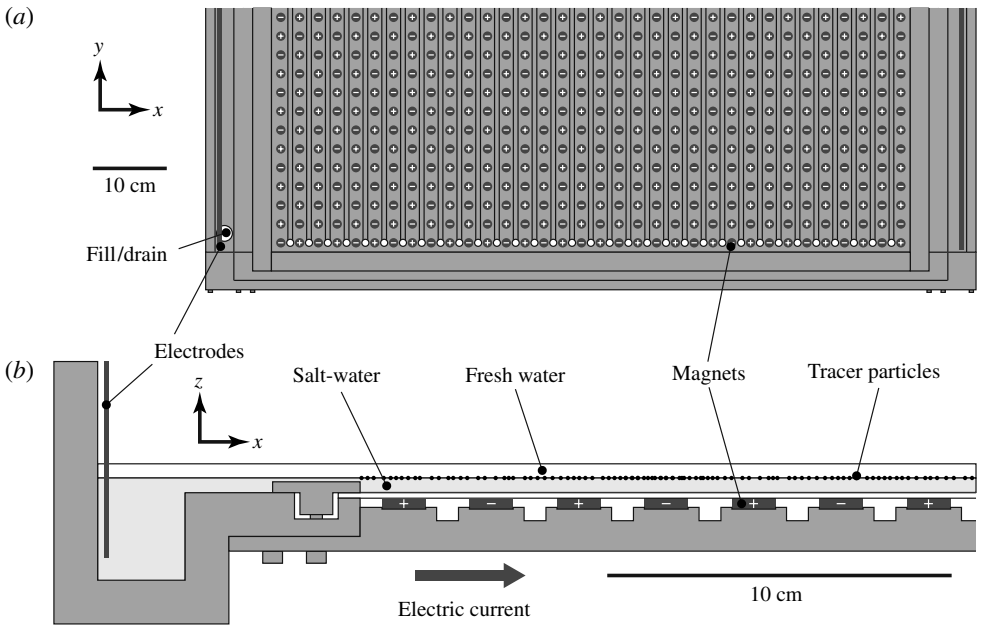


FIGURE 1. Schematic of the experimental apparatus, as seen (*a*) empty from above, and (*b*) filled in cross-section. Both panels are partial; the full test bed is square, with walls on all sides. DC electric current flows from left to right through the salt-water layer.

$$\Pi_S^{(r)} \equiv -\left[((u_i - u_i^{(r)})(u_j - u_j^{(r)}))^{(r)}\right] s_{ij}^{(r)}. \tag{2.9}$$

Below, we will consider these component fluxes in detail.

3. Experiment and data processing

To study the spectral energy fluxes as a function of space in an experiment, we must be able to measure the full velocity field and its gradients. In addition, to see non-negligible scale-to-scale energy flux, the nonlinear term in the Navier–Stokes equations must be strong; thus, the Reynolds number must be high, and the flow must be turbulent. But experimentally resolving the full time-resolved velocity field with sufficient resolution to measure the gradient in high-Reynolds-number laboratory turbulence remains an open problem; thus, we follow previous researchers and consider two-dimensional turbulence instead (Rivera *et al.* 2003; Chen *et al.* 2003, 2006; Kelley & Ouellette 2011*b*).

3.1. *Apparatus*

To generate quasi-two-dimensional flow, we drive a thin layer of electrolytic fluid using electromagnetic Lorentz forces. Our apparatus (shown in figure 1) is described in detail elsewhere (Kelley & Ouellette 2011*a*; Liao, Kelley & Ouellette 2012); we briefly review the set-up and parameters here.

Our working fluid is a very-high-aspect-ratio layer of salt water (16 % NaCl by mass dissolved in pure water) measuring 86 cm × 86 cm × 0.5 cm. The fluid sits on a glass bottom plate above a square array of permanent neodymium–iron–boron

https://doi.org/10.1017/jfm.2013.187 Published online by Cambridge University Press

magnets with magnetic fields of roughly 3000 Gauss at their surfaces. The magnets are arranged in a checkerboard pattern of alternating polarity, with a centre-to-centre spacing of 2.54 cm. The magnets themselves are discs with a diameter of 0.95 cm. We drive electric currents of up to a few amps laterally through the fluid (perpendicular to the magnetic field) between a pair of copper bar electrodes. The electric current and magnetic field together generate a nearly two-dimensional Lorentz body force that acts on the fluid and sets it into motion. The dominant length scale of this flow, and the scale L at which energy is injected, is set by the magnet spacing. We define a Reynolds number based on this scale and the root mean square (r.m.s.) velocity; note that this Reynolds number measures only the non-dimensional strength of the forcing rather than the extent of any turbulent cascades. We show data for two Reynolds numbers here: $Re = 185$, well above the transition to weak turbulence, and $Re = 38$, where the flow is nearly steady. We note that even at our higher Reynolds number, our flow does not show fully developed turbulence or extended energy or enstrophy cascades.

3.2. *Particle tracking*

To measure the flow field, we use particle tracking velocimetry (PTV), as we have described before (Kelley & Ouellette 2011*a*). We seed the fluid with small (51 μm in diameter) polystyrene particles that behave as passive tracers for this flow (Ouellette, O'Malley & Gollub 2008). The particles, with a specific gravity of 1.05, are less dense than the salt-water layer, and thus float to its surface. Once on the free surface, however, long-range, attractive surface-tension-driven forces would quickly cause the particles to clump together. To avoid this problem, we place a second fluid layer (also about 5 mm deep), this one of pure water, above the salt-water layer. Since the two fluids are miscible, there are no surface-tension forces to drive particle clustering. But since they are stably stratified, the two layers can remain distinct over the course of the experiment.

To image the particles, we use an IDT MotionPro M5 camera. The sensor measures 2320×1728 pixels, corresponding to an area of 31.7 cm $\times$ 23.6 cm (roughly $12L \times 9L$) in our flow. We image only the central region of the apparatus to avoid any possible wall effects. We typically locate about 30 000 particles at every instant of time. By recording images at a rate of 60 frames per second, we are able to follow the motion of even the fastest particles. The particles themselves are loaded with a dye that absorbs in the blue and emits in the green; we illuminate them with blue LEDs, and image them through an optical filter that removes the excitation wavelength so as to avoid glare from the fluid surface.

To measure the trajectories of each particle, we use a three-frame predictive best-estimate particle tracking algorithm that has been described in detail elsewhere (Ouellette, Xu & Bodenschatz 2006). We then calculate the Lagrangian velocities along the trajectories by convolving them with a Gaussian smoothing and differentiating kernel (Mordant, Crawford & Bodenschatz 2004).

3.3. *Velocity and flux fields*

Since the particles in our experiment are close together (compared with the dominant flow length scale L), we can compute the Eulerian velocity field by cubic interpolation between the locations of the Lagrangian points at each time step. We ensure that our velocity fields are reliably two-dimensional by projecting the measured flow fields onto a basis of numerically computed streamfunction eigenmodes (Kelley & Ouellette 2011*a*). An example of such a velocity field (down-sampled for clarity) is shown in

https://doi.org/10.1017/jfm.2013.187 Published online by Cambridge University Press

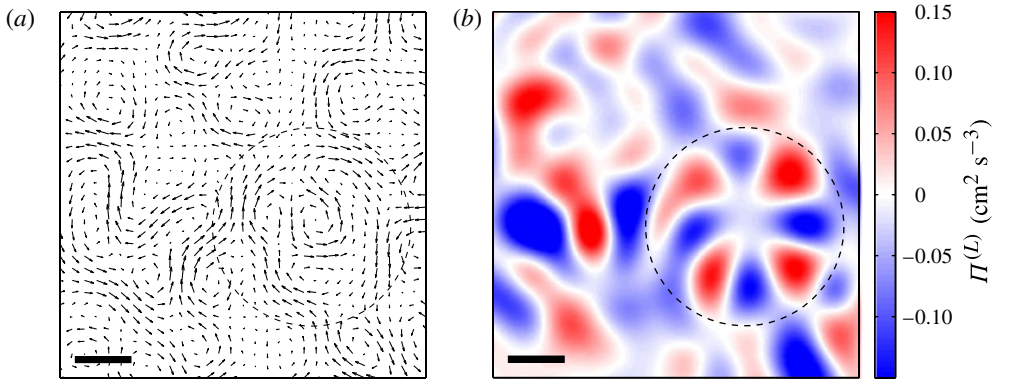


FIGURE 2. (Colour online) (*a*) Velocity field in a subregion of our measurement area at $Re = 185$. The field has been down-sampled for clarity, showing one velocity vector every 40 camera pixels (equivalent to one every 0.55 cm). The scale bar is $L = 2.54$ cm long. (*b*) Spectral energy flux for the same region and instant of time using a filter scale of $r = L$. Positive values denote transfer of energy to smaller length scales, while negative values mean transfer to larger scales. The dashed circle highlights a flux 'pinwheel' of alternating lobes with fourfold symmetry. Such pinwheels correspond to strong vortices in the flow field.

figure 2(*a*) for $Re = 185$. Although elements of the underlying vortex lattice are still evident at this Reynolds number, the flow is time-dependent and spatially disordered, with motion on many length and time scales.

In figure 2(*b*), we also show the spectral energy flux field $\Pi^{(L)}(\boldsymbol{x})$ for the same data set computed for the same instant of time and over the same region of space as the velocity field. For this example, we have used a filter scale of $r = L$ (the energy injection scale). We calculated the energy flux using the definitions given in § 2; to filter the velocity field and its products, we used a round Gaussian filter kernel. Other low-pass kernels give qualitatively similar, although not quantitatively identical, results (Rivera *et al.* 2003).

Like the velocity field, the spectral energy flux field is highly variable in space and time. It displays regions of both positive and negative flux (corresponding to downscale and upscale energy transport, respectively) even though the spatiotemporally averaged spectral flux is always positive at this filter scale (Kelley & Ouellette 2011*b*). In general, however, the spatial structure of the flux field is qualitatively uncorrelated with the velocity field, except for a few strong features. In figure 2, we indicate one such feature: a pattern of alternating lobes of positive and negative flux (here with fourfold rotational symmetry). These flux 'pinwheels' are often some of the strongest fluxes in the domain, and yet they average nearly to zero due to their symmetry. Thus, they make only a small contribution to the average energy cascade dynamics (Xiao *et al.* 2009). But if one attempts to study Lagrangian properties of the spectral flux field (Wan *et al.* 2010; Kelley & Ouellette 2011*b*), these pinwheels may matter quite a bit, since the lobes themselves are not material areas and thus fluid elements can pass in and out of them. Likewise, the pinwheels may potentially have a very large influence on attempts to link the spectral energy flux with coherent structures in the flow field (Ouellette 2012). Thus, we must ensure that we understand where they come from, and what their role is in the spectral transport.

Empirically, it seems that these flux pinwheels are associated with strong rotation in the flow (Xiao *et al.* 2009); their centres are nearly aligned with vortex cores.

https://doi.org/10.1017/jfm.2013.187 Published online by Cambridge University Press

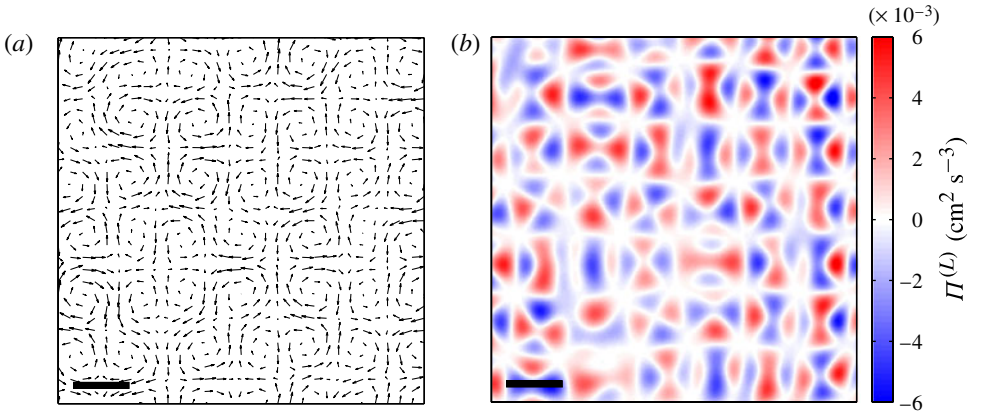


FIGURE 3. (Colour online) (*a*) Down-sampled velocity field for $Re = 38$, where the flow is nearly steady. The scale bar is again $L = 2.54$ cm long. (*b*) Corresponding spectral energy flux with a filter scale of $r = L$. Since the flow field is a vortex lattice at this Reynolds number, the flux field is a lattice of pinwheels.

Thus, to gain more insight, we also made measurements at a very low Reynolds number ($Re = 38$) where the flow field is nearly stationary and reflects the underlying magnet geometry. As shown in figure 3(*a*), under these conditions the flow field is a nearly regular square lattice of vortices of alternating sign. And, importantly, since the Reynolds number is very low, we would not expect significant spectral energy transport: such spectral flux is due solely to the action of the nonlinear term in the energy equation, which is weak relative to the direct viscous dissipation in low-Reynolds-number flow. We show the spectral energy flux computed for this low Reynolds number case in figure 3(*b*). Although the magnitude of the energy flux is certainly much lower than it is for the higher-Reynolds-number case, it does not vanish. In addition, the spectral flux field is very highly ordered in space: it is a lattice of flux pinwheels, mirroring the underlying vortex lattice. Nearly all of the measured spectral flux is carried by these pinwheels. And although the pinwheels may average away in Eulerian studies of the spectral transport (indeed, the spatial average of the flux field in figure 3(*b*) is nearly zero), as we discussed above their effect will be felt in Lagrangian measurements.

Two questions thus naturally arise. What is the origin of these flux pinwheels, and how can we distinguish their contribution from the rest of the spectral energy flux? To address these questions, we turn to a toy analytical model flow.

4. An example: steady cellular flow

To gain insight into these pinwheels, we work here with a simple example that we can address analytically. We consider a steady, two-dimensional cellular flow field given by the streamfunction

$$\Psi(x, y) = \frac{1}{\kappa} \sin \kappa x \sin \kappa y, \tag{4.1}$$

where κ is a wavenumber. This canonical flow field, sketched in figure 4, is frequently used for studying mixing, particularly when an oscillatory term is included (Solomon & Gollub 1988). As it has motion at only a single length scale (given by the inverse

https://doi.org/10.1017/jfm.2013.187 Published online by Cambridge University Press

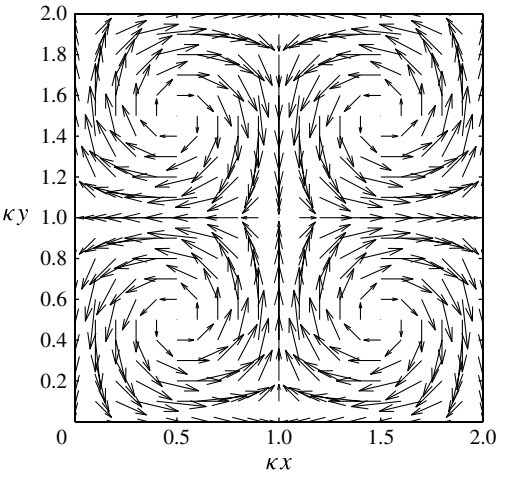


FIGURE 4. Velocity vectors in one unit cell of the cellular flow field defined by (4.1).

of κ) and has no dynamics in this steady form, we would not expect any spectral energy transport. Let us now apply a FST to this flow field to check this prediction.

4.1. *General results*

Before applying a FST to the cellular flow field, it will be useful to derive some general results. We can describe a generic two-dimensional incompressible flow field with a streamfunction

$$\Psi(\boldsymbol{x}) = \sum_n f_n \mathrm{e}^{\mathrm{i}\boldsymbol{k}_n\cdot\boldsymbol{x}} \equiv \sum_n \psi_n, \tag{4.2}$$

where we have expanded Ψ in Fourier modes. As usual, the velocity components are given by

$$u = \frac{\partial \Psi}{\partial y} = \sum_n ik_{n,y}\psi_n, \tag{4.3}$$

$$v = -\frac{\partial \Psi}{\partial x} = -\sum_n ik_{n,x}\psi_n, \tag{4.4}$$

where $k_{n,x}$, for example, is the x-component of wavevector $\boldsymbol{k}_n$.

For analytical convenience, we will use a round, sharp spectral filter, so that a single filtered Fourier mode is

$$\psi_n^{(r)} = \psi_n H(\kappa_r - |\boldsymbol{k}_n|), \tag{4.5}$$

where $\kappa_r = \pi/r$ is the filter cutoff wavenumber and H is the Heaviside step function, defined so that

$$H(\kappa_r - |\boldsymbol{k}_n|) = \begin{cases} 0, & |\boldsymbol{k}_n| > \kappa_r, \\ 1, & |\boldsymbol{k}_n| \leqslant \kappa_r. \end{cases} \tag{4.6}$$

To compute the spectral energy flux, we need to filter all of the terms appearing in (2.4). The quantities that are linear in the velocity are simple to handle, since

https://doi.org/10.1017/jfm.2013.187 Published online by Cambridge University Press

convolution is linear operation. We can thus immediately write

$$u^{(r)} = \sum_n ik_{n,y}\psi_n H(\kappa_r - |\boldsymbol{k}_n|), \tag{4.7}$$

$$v^{(r)} = -\sum_n ik_{n,x}\psi_n H(\kappa_r - |\boldsymbol{k}_n|), \tag{4.8}$$

$$\frac{\partial u^{(r)}}{\partial x} = -\sum_n k_{n,x}k_{n,y}\psi_n H(\kappa_r - |\boldsymbol{k}_n|), \tag{4.9}$$

$$\frac{\partial u^{(r)}}{\partial y} = -\sum_n k_{n,y}^2\psi_n H(\kappa_r - |\boldsymbol{k}_n|), \tag{4.10}$$

$$\frac{\partial v^{(r)}}{\partial x} = \sum_n k_{n,x}^2\psi_n H(\kappa_r - |\boldsymbol{k}_n|), \tag{4.11}$$

$$\frac{\partial v^{(r)}}{\partial y} = \sum_n k_{n,x}k_{n,y}\psi_n H(\kappa_r - |\boldsymbol{k}_n|). \tag{4.12}$$

The nonlinear terms are slightly more complicated, since we have to include two sums. We also have to take care to filter the *summed* wavevector. These terms are given by

$$(uu)^{(r)} = -\sum_{n,m} k_{n,y}k_{m,y}\psi_n\psi_m H(\kappa_r - |\boldsymbol{k}_n + \boldsymbol{k}_m|), \tag{4.13}$$

$$(vv)^{(r)} = -\sum_{n,m} k_{n,x}k_{m,x}\psi_n\psi_m H(\kappa_r - |\boldsymbol{k}_n + \boldsymbol{k}_m|), \tag{4.14}$$

$$(uv)^{(r)} = \sum_{n,m} k_{n,y}k_{m,x}\psi_n\psi_m H(\kappa_r - |\boldsymbol{k}_n + \boldsymbol{k}_m|). \tag{4.15}$$

Putting all of these terms together, we can write the total spectral energy flux through the scale r as

$$\begin{aligned}\Pi^{(r)} = \sum_{n,m,\ell} \psi_n\psi_m\psi_\ell \left\{ \left[k_{n,x}k_{m,x} - k_{n,y}k_{m,y}\right] k_{\ell,x}k_{\ell,y} - k_{n,y}k_{m,x}\left(k_{\ell,x}^2 - k_{\ell,y}^2\right)\right\} \\ \times H(\kappa_r - |\boldsymbol{k}_\ell|)\left\{H(\kappa_r - |\boldsymbol{k}_n + \boldsymbol{k}_m|) - H(\kappa_r - |\boldsymbol{k}_n|)H(\kappa_r - |\boldsymbol{k}_m|)\right\}.\end{aligned} \tag{4.16}$$

This expression can be simplified by defining

$$K_{nm\ell} \equiv \left[k_{n,x}k_{m,x} - k_{n,y}k_{m,y}\right] k_{\ell,x}k_{\ell,y} - k_{n,y}k_{m,x}\left(k_{\ell,x}^2 - k_{\ell,y}^2\right) \tag{4.17}$$

and

$$H_{nm\ell}^{(r)} = H(\kappa_r - |\boldsymbol{k}_\ell|)\left\{H(\kappa_r - |\boldsymbol{k}_n + \boldsymbol{k}_m|) - H(\kappa_r - |\boldsymbol{k}_n|)H(\kappa_r - |\boldsymbol{k}_m|)\right\}, \tag{4.18}$$

allowing us to write

$$\Pi^{(r)} = \sum_{n,m,\ell} \psi_n\psi_m\psi_\ell K_{nm\ell}H_{nm\ell}^{(r)}. \tag{4.19}$$

In these expressions, n and m index the wavevectors associated with the stress tensor $\tau_{ij}^{(r)}$, while ℓ indexes the wavevector associated with the filtered strain rate. Thus, this expression should be symmetric in n and m, which would amount to changing the

https://doi.org/10.1017/jfm.2013.187 Published online by Cambridge University Press

product uv to vu. As it stands, however, $K_{nm\ell}$ is not symmetric in n and m. Therefore, we explicitly symmetrize it, obtaining

$$\begin{aligned} K'_{nm\ell} &= (k_{n,x}k_{m,x} - k_{n,y}k_{m,y})k_{\ell,x}k_{\ell,y} - \tfrac{1}{2}(k_{n,x}k_{m,y} + k_{n,y}k_{m,x})\left(k_{\ell,x}^2 - k_{\ell,y}^2\right) \\ &= \tfrac{1}{2}(\boldsymbol{k}_n \cdot \boldsymbol{k}_\ell)|\boldsymbol{k}_m \times \boldsymbol{k}_\ell| + \tfrac{1}{2}(\boldsymbol{k}_m \cdot \boldsymbol{k}_\ell)|\boldsymbol{k}_n \times \boldsymbol{k}_\ell| \end{aligned} \tag{4.20}$$

giving, finally,

$$\Pi^{(r)} = \sum_{n,m,\ell} \psi_n \psi_m \psi_\ell K'_{nm\ell} H^{(r)}_{nm\ell}. \tag{4.21}$$

This expression tells us what wavevector triads contribute to the flux of energy through the filter scale r. Two factors are involved: $K'_{nm\ell}$ and $H^{(r)}_{nm\ell}$. Here $H^{(r)}_{nm\ell}$ directly tells us which wavenumbers are filtered away and therefore will not contribute to the flux. It clearly vanishes if $|\boldsymbol{k}_\ell| > \kappa_r$. If $|\boldsymbol{k}_m|$, $|\boldsymbol{k}_n|$ and $|\boldsymbol{k}_n + \boldsymbol{k}_m|$ are all larger than κ_r, the two terms in braces in (4.18) vanish independently, and thus so does $H^{(r)}_{nm\ell}$. If $|\boldsymbol{k}_m|$, $|\boldsymbol{k}_n|$ and $|\boldsymbol{k}_m + \boldsymbol{k}_n|$ are all less than or equal to κ_r, the two terms in braces in (4.18) cancel. For all other cases, however, $H^{(r)}_{nm\ell} = \pm 1$. On the other hand, $K'_{nm\ell}$ is essentially geometric: the relative orientations of $\boldsymbol{k}_m$, $\boldsymbol{k}_n$ and $\boldsymbol{k}_\ell$, and not their magnitudes, determine whether it will vanish. Note that $\boldsymbol{k}_m$ and $\boldsymbol{k}_n$ are associated with the stress tensor, while $\boldsymbol{k}_\ell$ is associated with the filtered rate of strain.

4.2. *Cellular flow*

We can now apply this calculation to the cellular flow field. We can write the Fourier representation of the streamfunction in (4.1) as

$$\Psi(\boldsymbol{x}) = \sum_{n=1}^{4} f_n \mathrm{e}^{\mathrm{i}\boldsymbol{k}_n \cdot \boldsymbol{x}} \tag{4.22}$$

with

$$f_1 = f_4 = -\frac{1}{4\kappa}, \tag{4.23}$$

$$f_2 = f_3 = \frac{1}{4\kappa} \tag{4.24}$$

and

$$\boldsymbol{k}_1 = \kappa\hat{\boldsymbol{x}} + \kappa\hat{\boldsymbol{y}}, \tag{4.25}$$

$$\boldsymbol{k}_2 = -\kappa\hat{\boldsymbol{x}} + \kappa\hat{\boldsymbol{y}}, \tag{4.26}$$

$$\boldsymbol{k}_3 = \kappa\hat{\boldsymbol{x}} - \kappa\hat{\boldsymbol{y}}, \tag{4.27}$$

$$\boldsymbol{k}_4 = -\kappa\hat{\boldsymbol{x}} - \kappa\hat{\boldsymbol{y}}, \tag{4.28}$$

where $\hat{\boldsymbol{x}}$ and $\hat{\boldsymbol{y}}$ are unit vectors in the two directions.

Let us choose a filter with a cutoff wavenumber of $\kappa_r = \sqrt{2}\kappa$. Given our definitions, this choice mean that all the step functions of the form $H(\kappa_r - |\boldsymbol{k}_n|)$ are equal to unity, although some (but not all) of the $H(\kappa_r - |\boldsymbol{k}_n + \boldsymbol{k}_m|)$ will vanish. Writing out the non-zero parts of the spectral flux and collecting terms yields

$$\Pi^{(r)} = -\kappa \cos\kappa x \cos\kappa y[\cos 2\kappa x - \cos 2\kappa y]. \tag{4.29}$$

Thus, we find that the flux of energy through κ_r does not vanish locally in this flow field, even though only one scale should be active. Consideration of the step

https://doi.org/10.1017/jfm.2013.187 Published online by Cambridge University Press

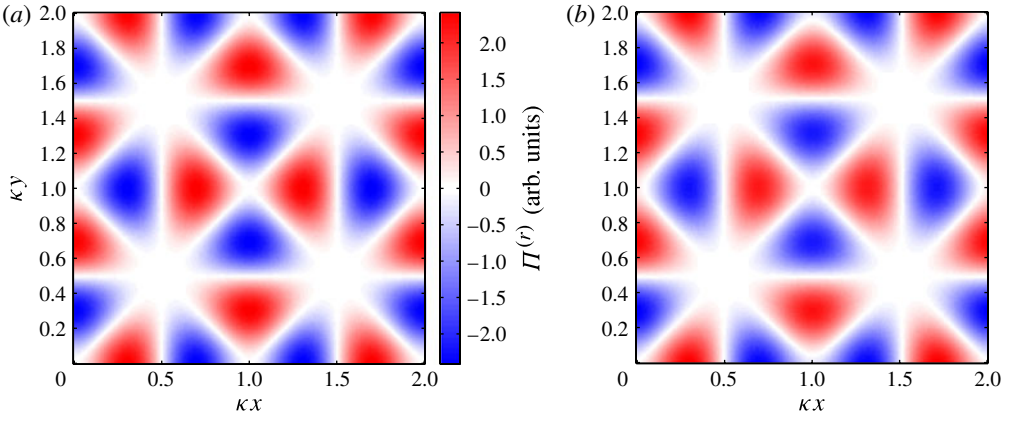


FIGURE 5. (Colour online) (*a*) Spectral energy flux (calculated analytically using a sharp spectral filter) in one unit cell of the cellular flow field, for $\kappa_r = \sqrt{2}\kappa$. (*b*) Spectral energy flux for the same cellular flow field computed numerically using the Gaussian filter we use for the experimental data. The colour scale is the same for both panels.

functions involved shows that this result holds for all wavenumber cutoffs in the range $\sqrt{2}\kappa \leqslant \kappa_r < 2\kappa$. We plot this non-vanishing flux in figure 5; note that it has the same pinwheel characteristics as we observed from our experiments in figure 3, and that the average over all space does vanish. For comparison, we also show in figure 5 the spectral flux from the steady cellular flow analysed numerically (rather than analytically) with the same Gaussian filter we use to process the experimental data, with results that are qualitatively similar to the analytical case. These results leave us in a quandary: what is the source of this unexpected spectral flux?

4.3. *Flux decomposition*

As discussed above, the stress tensor $\tau_{ij}^{(r)}$ can be decomposed into three logically distinct pieces; in analogy with LES, we can call them the Leonard stress, cross stress and subgrid stress. This decomposition in turn allows us to split the spectral energy flux into three pieces as well, which we labelled above as $\Pi_L^{(r)}$, $\Pi_C^{(r)}$ and $\Pi_S^{(r)}$. Let us now consider these three terms in the context of the cellular flow we have presented here.

In the framework we presented in § 4.1, the decomposition into these three component fluxes only affects the Heaviside functions, leaving the geometric term unchanged. It is straightforward to show that for a generic two-dimensional incompressible flow

$$\Pi_L^{(r)} = -\sum_{nm\ell} \psi_n \psi_m \psi_\ell K'_{nm\ell} H_\ell H_n H_m (1 - H_{nm}), \tag{4.30}$$

$$\Pi_C^{(r)} = \sum_{nm\ell} \psi_n \psi_m \psi_\ell K'_{nm\ell} H_\ell H_{nm} (H_n + H_m - 2H_n H_m), \tag{4.31}$$

$$\Pi_S^{(r)} = \sum_{nm\ell} \psi_n \psi_m \psi_\ell K'_{nm\ell} H_\ell H_{nm} (1 - H_n)(1 - H_m), \tag{4.32}$$

https://doi.org/10.1017/jfm.2013.187 Published online by Cambridge University Press

where we have introduced the shorthand notation

$$H_n \equiv H(\kappa_r - |\boldsymbol{k}_n|) \tag{4.33}$$

and

$$H_{nm} \equiv H(\kappa_r - |\boldsymbol{k}_n + \boldsymbol{k}_m|). \tag{4.34}$$

If we now go back to our cellular flow example, it is straightforward to show that $\Pi_C^{(r)}$ and $\Pi_S^{(r)}$ vanish for all choices of filter scale r, as should be expected for this flow field. The entire contribution in (4.29) is due to the Leonard term $\Pi_L^{(r)}$.

What is the origin of this effect? As we discussed above, the Leonard term contains only contributions from the filtered velocity field. Thus, logically, it represents the transfer of energy between large-scale modes that are retained in the velocity field after filtering. The key to understanding why we see non-zero spectral flux from the Leonard term in this cellular flow thus lies in (4.22): even though there is energy at only a single wavenumber (κ) in this flow, it takes four linearly independent wavevectors to specify the flow field. Each of these wavevectors is retained in the flow field after filtering (in the range where the Leonard term is non-zero), and so the Leonard term tells us about the exchange of energy between these modes. This argument also explains the pinwheel shape of the flux fields: the flux vanishes at the 45° lines in the flow where the contribution of a pair of wavevectors is exactly balanced, but is non-zero whenever the contribution of one wavevector to the local flow is larger than another. This same behaviour will occur around any strong vortex core, as indeed we see in the experimental spectral energy flux fields.

Let us now return to experimental data and study the decomposition of the spectral energy flux there.

5. Analysis of experimental velocity fields

Our analysis of the cellular flow field suggests that the Leonard term may be responsible for the pinwheels we saw in figures 2 and 3. And, since we did not expect to find any flux in the single-scale cellular flow example, our results further suggest that the pinwheels do not in fact tell us about the transfer of energy between scales. Let us now look back at our experimental data to test these hypotheses.

5.1. *Spectral flux fields*

As described above in § 3.3, we calculated the spectral energy flux from our measured velocity fields using a round Gaussian low-pass filter kernel. In figure 6(*a*), we show a single spectral energy flux field for $Re = 185$, computed using a filter scale of $r = 1.5L$ (where the average flux is largest). We also show, in figure 6(*b–d*), Π_L, Π_C and Π_S. Unlike in the cellular flow case, none of these three terms vanishes, as should be expected given that at this Reynolds number the flow is weakly turbulent. We therefore expect nonlinear scale-to-scale energy transfer to be acting. But the spatial structure of these three terms is very different. Inspection of the Leonard term Π_L shows the same kind of pinwheel structures we saw around vortices in § 3.3; compare, for example, with figures 2(*b*) and 3(*b*). These pinwheels are much less apparent in the cross term, if they are there at all, and wholly absent in the subgrid term. By analogy with the cellular flow results, our data thus suggest that the pinwheels, and perhaps the entire Leonard term, does not contribute meaningfully to the scale-to-scale energy flux, but instead arises due to the mixing of differently oriented but resolved wavevectors.

https://doi.org/10.1017/jfm.2013.187 Published online by Cambridge University Press

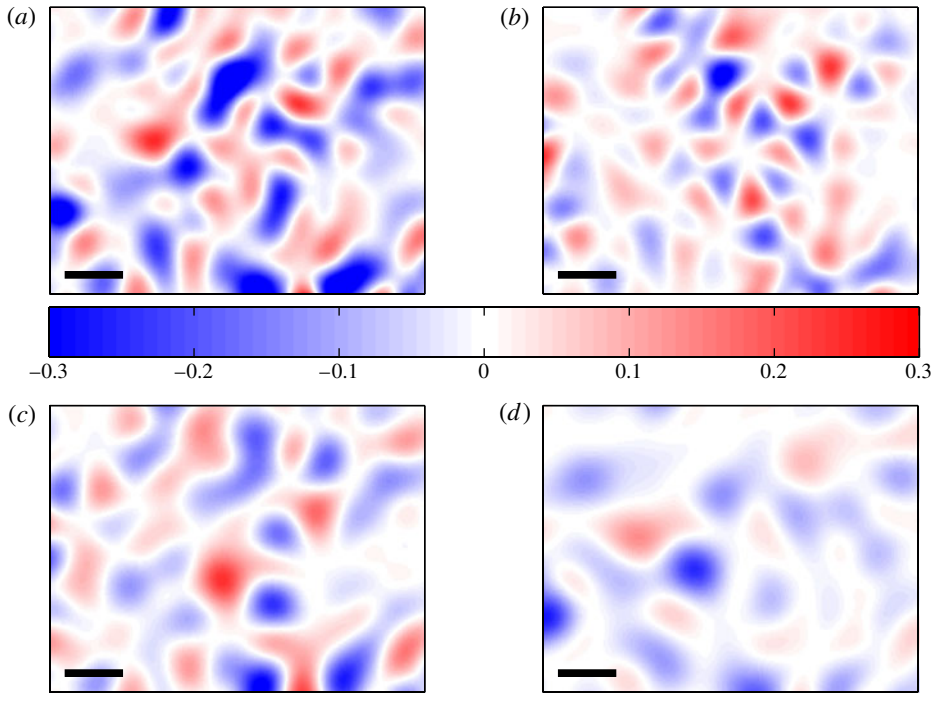


FIGURE 6. (Colour online) Spectral energy flux at $Re = 185$ calculated with a filter scale of $r = 1.5L$: (*a*) full $\Pi^{(1.5L)}$; (*b*) Leonard term $\Pi_L^{(1.5L)}$; (*c*) cross term $\Pi_c^{(1.5L)}$; (*d*) subgrid term $\Pi_S^{(1.5L)}$. The colour scale is the same for all panels and the scale bar is $L = 2.54$ cm long. Note that the Leonard term contains the bulk of the pinwheel structures.

These results are further borne out by decomposing the spectral flux measured in the low-Reynolds-number ($Re = 38$) case, as shown in figure 7. Bright pinwheels are very obvious in the Leonard term, and weaker versions also appear in the cross term. Although the subgrid term also displays the symmetries of the flow field (as it must, at this Reynolds number), pinwheel structures are not present.

5.2. *Spatially averaged flux*

Our interpretation of the three decomposed spectral fluxes is bolstered by considering their spatiotemporal averages. The average value of the energy flux $\Pi^{(r)}$ should in principle be straightforward to interpret in an inverse energy cascade scenario. We would expect $\langle \Pi^{(r)} \rangle$ to be constant and negative in the inertial range of the inverse cascade, and zero everywhere else.

To measure such averages, we calculated many individual spectral flux fields (such as those shown in figure 6) at instants of time that were separated by more than the large-eddy turnover time of the flow field, so that they could be considered to be statistically independent. We then averaged each field over space, and then averaged all of these spatial mean values over the ensemble of different times. The results are shown in figure 8(*a*), for our higher Reynolds number. As is typical for this kind of experiment (Rivera *et al.* 2003; Kelley & Ouellette 2011*b*), we find a negative region for scales larger than the forcing scale L, and a positive 'backscatter' region (denoting downscale transport) at scales comparable to and smaller than L. There are no regions

https://doi.org/10.1017/jfm.2013.187 Published online by Cambridge University Press

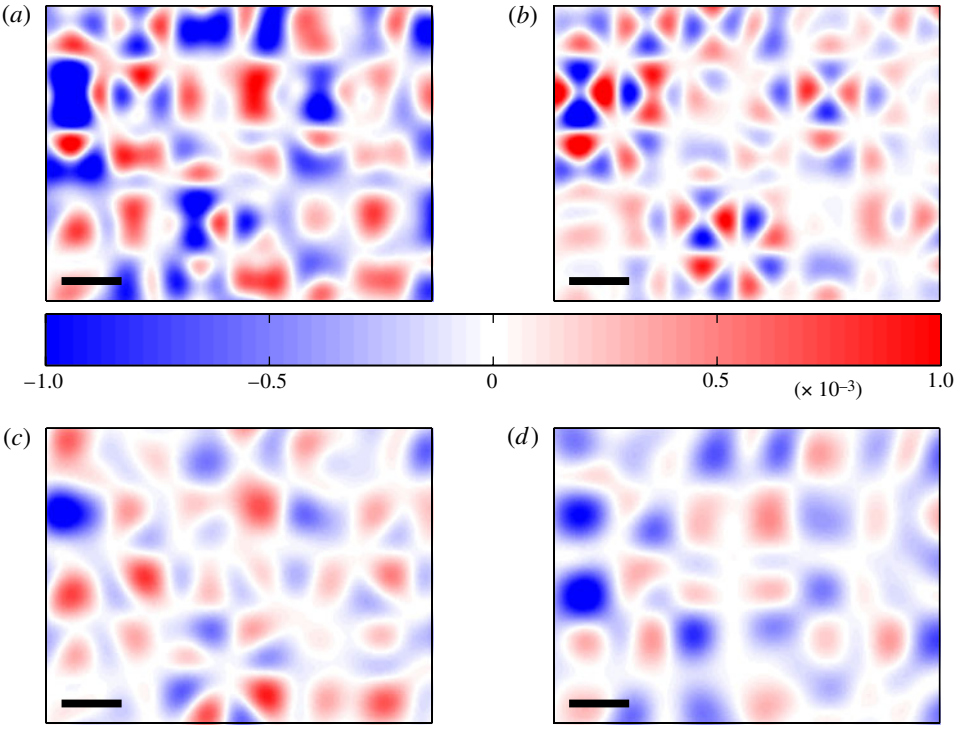


FIGURE 7. (Colour online) Spectral energy flux at $Re = 38$ calculated with a filter scale of $r = 1.5L$: (*a*) full $\Pi^{(1.5L)}$; (*b*) Leonard term $\Pi_L^{(1.5L)}$; (*c*) cross term $\Pi_c^{(1.5L)}$; (*d*) subgrid term $\Pi_S^{(1.5L)}$. The colour scale is the same for all panels and the scale bar is $L = 2.54$ cm long.

of constant flux (corresponding to inertial ranges) in our data since the Reynolds number is not high enough for the turbulence to have reached its asymptotic, fully developed state.

In figure 8(*a*), we also show the averages of the three component fluxes $\Pi_L^{(r)}$, $\Pi_C^{(r)}$ and $\Pi_S^{(r)}$. The Leonard term, which as we have shown above contains the majority of the pinwheel structures, has a near-zero spatiotemporal average at scales larger than L, and only contributes meaningfully to the backscatter peak.

The average of the cross term $\Pi_C^{(r)}$ behaves similarly to the Leonard term, though with a slightly higher magnitude. It contributes little to the expected inverse energy transfer, is the dominant part of the backscatter peak, and has an effect only very near the forcing scale.

Finally, we consider the average of the subgrid term $\Pi_S^{(r)}$. Here, we find what would be expected in the simplest double-cascade picture of two-dimensional turbulence. The subgrid flux, which has no apparent pinwheels, is always negative; that is, it always shows inverse energy transfer. Thus, the subgrid term appears to be the dominant driver of the inverse energy cascade.

In figure 8(*b*), we show the spatially averaged total and component fluxes for our lower-Reynolds-number case. As expected, the overall flux is significantly reduced at this Reynolds number (by three orders of magnitude, compared with the higher-Reynolds-number case). But the overall trends we observed at higher Reynolds number

https://doi.org/10.1017/jfm.2013.187 Published online by Cambridge University Press

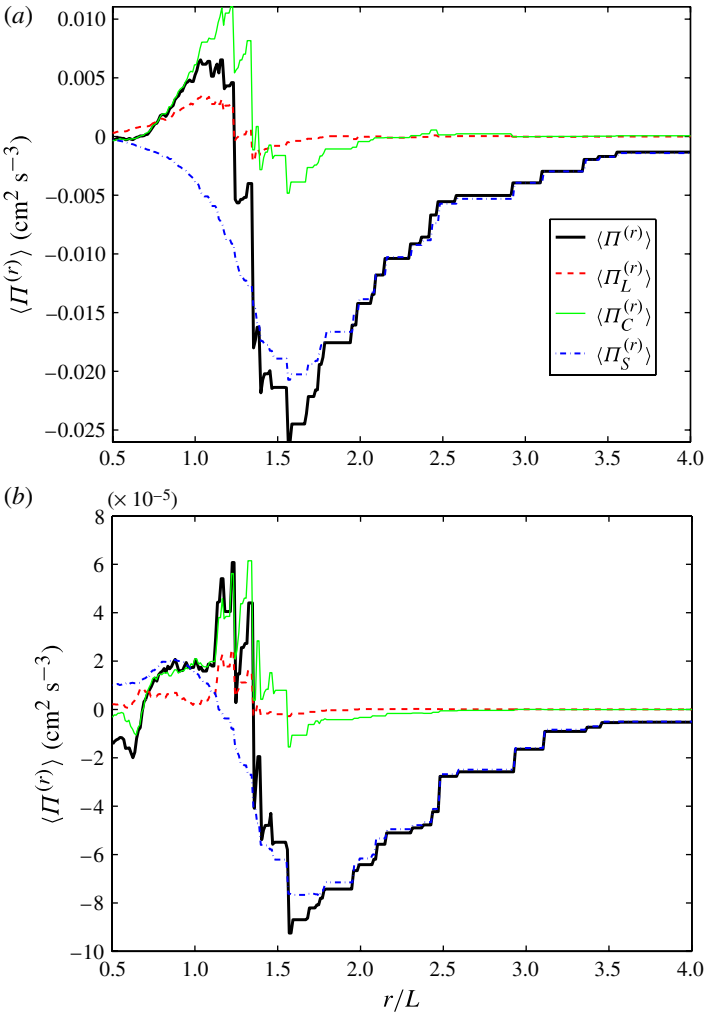


FIGURE 8. (Colour online) Spatiotemporally averaged spectral energy fluxes for (*a*) $Re = 185$ and (*b*) $Re = 38$. For both Reynolds numbers, the Leonard term and cross term are significant only near the forcing scale L, and account for nearly all of the positive flux. The subgrid flux accounts for nearly all of the inverse energy transfer.

persist here: the contributions of the Leonard flux and cross flux are localized near the forcing scale, where the vortex structure of the flow is most evident, and the subgrid flux carries most of the inverse energy transfer.

6. Summary and conclusions

We have studied the spatial structure of the scale-to-scale energy flux in two-dimensional flow using FSTs, using both a simple analytical model and a quasi-two-dimensional weakly turbulent experimental flow. As had previously been noted by other researchers, we found patterns of alternating lobes of intense spectral energy flux, which we termed flux pinwheels, associated with strong vortices in the flow field. Although the contribution of these pinwheels tends to be negligible when considering

https://doi.org/10.1017/jfm.2013.187 Published online by Cambridge University Press

spatial averages of the spectral energy flux (due to their symmetry), they may have a non-trivial impact on both Lagrangian statistics (since the pinwheels are not material areas) and on attempts to correlate coherent structures in the flow field with the spectral energy flux.

To understand the origin of these pinwheels, we decomposed the scale-to-scale flux into three components: a Leonard term (representing the interaction of two large-scale modes), a cross term (representing the interaction of one large- and one small-scale mode) and a subgrid term (representing the interaction of two small-scale modes). In our simple cellular flow example, all of the measured spectral flux, which was expected to vanish, came from the Leonard term. Likewise, in our experimental data sets, we showed that the majority of the flux pinwheels were associated with the Leonard term. Both of these results suggest that the interpretation of the Leonard term is subtle. Although it does represent the transfer of energy between modes in the flow field, the Leonard term does not measure the transfer between large and small scales; rather, it appears to be dominated by the transfer of energy between different resolved wavevectors. In contrast, the subgrid term shows no evidence of pinwheels, and its spatial average is entirely consistent with the inverse energy cascade expected in two-dimensional turbulence (unlike the Leonard term and cross term, which are active over only a small range of scales and contributes primarily to forward energy transfer).

Acknowledgements

We thank D. Kelley for his help with the experiments and for developing the analysis software. This work was supported by the U.S. National Science Foundation under grant numbers DMR-0906245 and DMR-1206399.

REFERENCES

BATCHELOR, G. K. 1969 Computation of the energy spectrum in homegeneous two-dimensional turbulence. *Phys. Fluids* **12**, II233–II239.

BOFFETTA, G. 2007 Energy and enstrophy fluxes in the double cascade of two-dimensional turbulence. *J. Fluid Mech.* **589**, 253–260.

BOFFETTA, G. & ECKE, R. E. 2012 Two-dimensional turbulence. *Annu. Rev. Fluid Mech.* **44**, 427–451.

BOFFETTA, G. & MUSACCHIO, S. 2010 Evidence for the double cascade scenario in two-dimensional turbulence. *Phys. Rev.* E **82**, 016307.

CHEN, S., ECKE, R. E., EYINK, G. L., RIVERA, M., WAN, M. & XIAO, Z. 2006 Physical mechanism of the two-dimensional inverse energy cascade. *Phys. Rev. Lett.* **96**, 084502.

CHEN, S., ECKE, R. E., EYINK, G. L., WANG, X. & XIAO, Z. 2003 Physical mechanism of the two-dimensional enstrophy cascade. *Phys. Rev. Lett.* **91**, 214501.

EYINK, G. L. 1995 Local energy flux and the refined similarity hypothesis. *J. Stat. Phys.* **78**, 335–351.

GERMANO, M. 1992 Turbulence: the filtering approach. *J. Fluid Mech.* **238**, 325–336.

HUSSAIN, A. K. M. F. 1986 Coherent structures and turbulence. *J. Fluid Mech.* **173**, 303–356.

KELLEY, D. H. & OUELLETTE, N. T. 2011*a* Onset of three-dimensionality in electromagnetically forced thin-layer flows. *Phys. Fluids* **23**, 045103.

KELLEY, D. H. & OUELLETTE, N. T. 2011*b* Spatiotemporal persistence of spectral fluxes in two-dimensional weak turbulence. *Phys. Fluids* **23**, 115101.

KRAICHNAN, R. H. 1967 Inertial ranges in two-dimensional turbulence. *Phys. Fluids* **10**, 1417–1423.

LEITH, C. E. 1967 Diffusion approximation for two-dimensional turbulence. *Phys. Fluids* **11**, 671–673.

https://doi.org/10.1017/jfm.2013.187 Published online by Cambridge University Press

LIAO, Y., KELLEY, D. H. & OUELLETTE, N. T. 2012 Effects of forcing geometry on two-dimensional weak turbulence. *Phys. Rev.* E **86**, 036306.

LIU, S., MENEVEAU, C. & KATZ, J. 1994 On the properties of similarity subgrid-scale models as deduced from measurements in a turbulent jet. *J. Fluid Mech.* **275**, 83–119.

MENEVEAU, C. & KATZ, J. 2000 Scale-invariance and turbulence models for large-eddy simulation. *Annu. Rev. Fluid Mech.* **32**, 1–32.

MORDANT, N., CRAWFORD, A. M. & BODENSCHATZ, E. 2004 Experimental Lagrangian probability density function measurement. *Physica* D **193**, 245–251.

OUELLETTE, N. T. 2012 On the dynamical role of coherent structures in turbulence. *C. R. Physique* **13**, 866–877.

OUELLETTE, N. T., O'MALLEY, P. J. J. & GOLLUB, J. P. 2008 Transport of finite-sized particles in chaotic flow. *Phys. Rev. Lett.* **101**, 174504.

OUELLETTE, N. T., XU, H. & BODENSCHATZ, E. 2006 A quantitative study of three-dimensional Lagrangian particle tracking algorithms. *Exp. Fluids* **40**, 301–313.

POPE, S. B. 2000 *Turbulent Flows*. Cambridge University Press.

RIVERA, M. K., DANIEL, W. B., CHEN, S. Y. & ECKE, R. E. 2003 Energy and enstrophy transfer in decaying two-dimensional turbulence. *Phys. Rev. Lett.* **90**, 104502.

SOLOMON, T. H. & GOLLUB, J. P. 1988 Chaotic particle transport in time-dependent Rayleigh–Bénard convection. *Phys. Rev.* A **38**, 6280–6286.

WAN, M., XIAO, Z., MENEVEAU, C., EYINK, G. L. & CHEN, S. 2010 Dissipation-energy flux correlations as evidence for the Lagrangian energy cascade in turbulence. *Phys. Fluids* **22**, 061702.

XIAO, Z., WAN, M., CHEN, S. & EYINK, G. L. 2009 Physical mechanism of the inverse energy cascade of two-dimensional turbulence: a numerical investigation. *J. Fluid Mech.* **619**, 1–44.

https://doi.org/10.1017/jfm.2013.187 Published online by Cambridge University Press